DOI: 10.1002/((please add manuscript number))
**Article type: Communication**

# Magnetic interaction of multifunctional core-shell nanoparticles for highly effective theranostics

*Ming-Da Yang, Chien-Hsin Ho, Sergiu Ruta, Roy Chantrell, Kathryn Krycka, Ondrej Hovorka, Fu-Rong Chen, Ping-Shan Lai, and Chih-Huang Lai**

[*] Prof. C.-H. Lai, M. D. Yang, Dr. C. H. Ho.
Department of Materials Science and Engineering, National Tsing Hua University, No. 101, Section 2, Kuang-Fu Road, Hsinchu, Taiwan 30013, R.O.C.
E-mail: chlai@mx.nthu.edu.tw
Prof. R. Chantrell, Dr. S. Ruta,
Department of Physics, the University of York, York YO10 5DD, UK
Dr. K. Krycka
The Centre for High Resolution Neutron Scattering, National Institute of Standards and Technology, United States
Prof. O. Hovorka
Engineering and the Environment, University of Southampton, Southampton SO16 7QF, UK
Prof. Fu-Rong Chen
Department of Engineering and System Science, National Tsing Hua University, No. 101, Section 2, Kuang-Fu Road, Hsinchu, Taiwan 30013, R.O.C.
Prof. Ping-Shan Lai
Department of Chemistry, National Chung Hsing University, No. 145 Xingda Rd., South Dist., Taichung City 402, Taiwan

Keywords: magnetic resonance image, hyperthermia, theranostics, core-sell, magnetic interaction

Controlled-size and surface treatment of magnetic nanoparticles (NPs) make one-stage combination feasible for enhanced magnetic resonance image (MRI) contrast and effective hyperthermia. However, superparamagnetic behavior, essential for avoiding aggregation of magnetic NPs, substantially limits their performance. Here, we developed a superparamagnetic core-shell structure, which promotes the formation of vortex-like intra-particle magnetization structures in the remanent state leading to reduced dipolar interactions between two neighboring NPs, while during MRI scan, the presence of DC magnetic field induces formation of NP chains, introducing increased local inhomogeneous dipole fields which enhance relaxivity. The core-shell NPs also reveal an augmented anisotropy, due to exchange coupling to the high anisotropy core, which enhances the specific absorption rate.

Our *in-vivo* tumor study reveals that the tumor cells can be clearly diagnosed during MRI scan and the tumor size is substantially reduced through hyperthermia therapy by using the same FePt@IONPs, realizing the concept of theranostics

One of the current challenges in biomedical science is that of developing multifunctional materials with functionality for both ultrasensitive imaging and highly effective therapy. Magnetic nanoparticles (NPs) have been widely used as magnetic resonance imaging (MRI) contrast agents. When an external magnetic field is applied, the magnetic NPs that label cells cause a significant dephasing of protons due to the magnetic field inhomogeneity induced in the water molecules within the cells [1]. Magnetic NPs also provide a promising application in cancer therapy through magnetic hyperthermia, which utilizes the heat generated by magnetic NPs under an alternating field to kill tumor cells [1-3]. Magnetic NPs injected into the body for diagnosis could also be used in subsequent therapy. The concept of theranostics (a combination of diagnosis and therapy) would be highly advantageous to medicine as the same particles can be used for detection and for treatment of tumors [4]. However, magnetic NPs serving as theranostic agents are still in an early stage of development.

Iron oxide nanoparticles (IONPs) have been considered a promising candidate for an MRI contrast and cancer treatment with hyperthermia due to their bio-compatibility. The typical relaxivity and specific absorption rate (SAR) of iron oxide-based magnetic NPs range from 100 to 200 $S^{-1}$ $mMFe^{-1}$ and 100 to 500 W/g, respectively, and still require further improvement to reduce the required dosage for clinical usage [1, 2]. Several approaches for optimizing the MRI contrast of IONPs have been demonstrated by varying their composition (saturation magnetization) [5-9], surface treatment [8-13], or size [5-9]. As for the SAR, power dissipation can be enhanced by tuning magnetic anisotropy, particle size or saturation magnetization [14, 15]. To extend the functionality and overcome the limitations of single-

component magnetic NPs, the magnetic core can be selectively modified to compliment the properties of the shell. The magnetic core-shell structure, which possesses tunable magnetic anisotropy and magnetization, has been demonstrated to achieve contrast-enhanced MRI [16,17] or efficient heat induction [14]. However, very limited reports so far demonstrate superparamagnetic NPs for highly effective theranostics, that is, enhanced $r_2$ and SAR simultaneously.

Regarding MRI contrast, $r_2$ relaxivity has been reported to depend on the properties of a single magnetic particle based on outer-sphere relaxation theory [18]. However, during the MRI process, a strong DC magnetic field is applied to align the protons, and a small AC field is used to disturb their alignment, contributing to $T_2$ relaxation due to local variations in precession rate. Therefore, magnetic NPs may interact with each other in the presence of magnetic fields and form various forms of clusters or assemblies. So far, no related investigations have addressed how magnetic interactions between NPs influence the formation of clusters or assemblies under magnetic fields. Likewise, the effect on $T_2$-weighted MRI has not yet been discussed.

Here, we demonstrate the importance of the magnetic interaction between NPs for both the relaxivity and the SAR, which provides a new tuning knob for NP designs used for MRI and hyperthermia. By using core-shell superparamagnetic NPs composed of FePt core protected by a biocompatible cubic $Fe_3O_4$ shell, we can tune magnetic interactions among NPs as well as between the core and shell. The monodispersed FePt@IONPs are shown to simultaneously possess highly effective $T_2$-shorting ($r_2$=360 $mM^{-1}s^{-1}$) and high-efficiency hyperthermia (SAR=1.21 kW/g), which enables therapy immediately after a diagnosis using the same NPs.

Cubic FePt@IONPs show a high $r_2$ relaxivity of 360 $mM^{-1}s^{-1}$ at 4.7 T, while the $r_2$ relaxivity of cubic IONPs and Resovist® are lower, at 129 $mM^{-1}s^{-1}$ and 194 $mM^{-1}s^{-1}$ (**Figure 1a**). The FePt@IONP nanocubes also show significantly darkened phantom images, as shown in Figure 1b, which correspond to a strongly enhanced $T_2$ contrast relative to the cubic IONPs and Resovist® NPs. Resovist® and our cubic IONPs show SAR values of 0.39 kW/g and 0.92 kW/g, respectively, while FePt@IONPs exhibits a value of 1.21 kW/g (Figure 1c). (See Supplementary Section 1 for details of the SAR calculations of NPs.) For the cancer hyperthermia treatment, the temperature needs to be increased to 42 $^oC$. Because of the high SAR, the required dose and exposure time to reach 42 $^oC$ in the in-vitro experiment are only 0.1 mg/ml of FePt@IONPs and 100 sec, respectively, measured with an AC magnetic field of 18.8 kA/m at 630 kHz and with dispersion volume of 0.2ml. For the *in-vivo* theranostic demonstrations presented here, MRI was acquired with a quadrature surface coil using a spin echo sequence with DC magnetic field, and magnetic hyperthermia was applied with an AC magnetic field provided by a magnetic induction local coil with a diameter of 3 cm [19] (Figure 1d). Theranostic application of core-shell FePt@IONPs was carried out in KB human cervical cancer cells xenografted mice model. FePt@IONPs were intravenously injected into mice at 0.1 mg/ml with the dispersion volume of 0.2ml; 24 hrs later, the mice were placed in a 3-T MRI head coil and subsequently under the magnetic induction local coil for magnetic hyperthermia. The tumor MR contrast ability of FePt@IONP is about 1.5 times higher than that of Resovist® (Figure 1e). Note that the different mice may exhibit different background MR signals in tumor areas. In our tumor MR contrast, we compare the contrast in tumor area with background in the same mice so that we can do fair comparison for MRI contrast with different contrast agents [20]. We also compare MR images taken at kidney and liver before and after intravenous injection of FePt@IONPs, shown in **Figure S1**. We can clearly observe the enhanced contrast after the injection of FePt@IONP. For magnetic hyperthermia, the tumor area was treated with an AC magnetic field of 18.8 kA/m at 630 kHz for 10 min and

the tumor size was monitored for up to half a month. Significant delay of tumor growth was observed in FePt@IONP hyperthermia group at day 15 whereas Resovist® hyperthermia group revealed no inhibition of tumor growth compared with untreated control group (neither NPs nor hyperthermia treatment) (Figure 1f). Note that the tumor volume still increases for the FePt@IONP control sample (with FePt@IONP but without hyperthermia), which clearly indicates that FePt@IONPs show efficient magnetic hyperthermia treatment of the cancer due to their high SAR. Furthermore, the increased tumor volume in the FePt@IONP control sample also suggests that cytotoxicity of FePt@IONP is not severe. Clear MRI images of NPs can accurately locate the tumor region where the same NPs can be used for highly effective hyperthermia to realize the theranostic modality of precise diagnosis and treatment.

To extend the functionality and overcome the limitations of single-component magnetic NPs, the magnetic core can be selectively modified to compliment the properties of the shell. **Figure 2a** shows the transmission electron microscopy (TEM) image of $Fe_3O_4$ nanocubes. The average edge length of $Fe_3O_4$ cubes is 16.1 ± 0.9 nm and that of the bi-magnetic core-shell FePt@IONPs with FePt core and cubic shell $Fe_3O_4$ is 14.7 ± 1.1 nm (Figure 2b). The disordered FePt NPs are spherical, exhibiting superparamagnetic behavior due to their small size of about 4.1 nm. The high-quality single-crystalline structure of the nanocubes is shown in Figure 2c. The FePt core obviously embedded inside the cubes was demonstrated by aligning a tilt series in three-dimensional (3D) TEM tomography (Figure 2c). The XRD patterns of the nanocube assembly on Si substrates indicate that our IONP structure corresponds to the $Fe_3O_4$ lattice (**Figure S2a-c**). The X-ray photoelectron spectra (XPS) of IONPs and FePt@IONPs also show no satellite peak between the peaks of Fe $2p_{3/2}$ and Fe $2p_{1/2}$, indicating that these nanocubes are consistent with the $Fe_3O_4$ component (Figure S2e, f).

Before discussing the mechanism of superior performance of the FePt@INOPs in both MRI contrast and hyperthermia, we first evaluated the cytotoxicity and stability of FePt@INOPs dispersed in water. To demonstrate the effects of magnetic interaction of NPs on MRI contrast, we specifically used a surfactant with short-chain molecules, CTAB (hexadecylcetyltrimethylammonium bromide, FW: 364.45), a well-known surfactant for dispersing and stabilization of NPs. On the other hand, CTAB-stabilized NPs used for bio-applications may cast doubts about their cytotoxicity. Therefore, we also used mPEG (methoxy-polyethylene glycol, FW: 350) as a surfactant. The mPEG coated IONP is widely used for bio-application and reveals no cytotoxicity [21]. The selected mPEG possesses similar molecular weight to CTAB and its short-chain molecule does not significantly change the hydrodynamic diameter, therefore, mPEG-coated NPs may provide the similar magnetic interactions among NPs to CTAB-coated NPs. The enhancements of $r_2$ and SAR by using mPEG-coated FePt@IONPs (Figure. S3) are similar to those shown in Figure 1, by using CATB-coated FePt@IONPs. Figure S4 and S5 show MTT assay for KB cells and H&E staining of major organs after the magnetic hyperthermia treatment, respectively. Both results clearly demonstrate that mPEG-coated FePt@IONPs have no toxic reaction for KB cells and organs. In addition, dynamic light scattering (DLS) data reveal that the particle size for monodisperse FePt@IONP and IONP does not change significantly after 24 hrs (**Figure S6**), indicating no aggregation occurs. All results clearly demonstrate that our FePt@IONP can be directly applied to MRI and hyperthermia without concerns of cytotoxicity and stability.

The hysteresis loops for nanocubes in water (**Figure 3a**) reveal that both cubic IONPs and FePt@IONPs exhibit superparamagnetic behavior at room temperature. The theoretical saturation magnetizations of bulk $Fe_3O_4$ and FePt are 471 emu/cc and 1140 emu/cc, respectively. The FePt core does not contribute significantly to the magnetic moment as it accounts for merely 1% of the volume of the magnetic structure. When the proton diffusion

length is not negligible with respect to the size of NPs, the MRI relaxivity can be described in the motional averaging regime of protons. The relaxivity is expected to be directly proportional to the NP size squared and to the saturation magnetization. [22, 23] Also, the SAR value is expected to be linearly dependent on the saturation magnetization for superparamagnetic NPs[1]. Since our cubic IONPs and FePt@IONPs have similar sizes and saturation magnetization, the enhanced contrast and heating efficiency of FePt@IONPs in comparison to IONPs cannot be attributed to these two factors. A slight increase of coercivity for FePt@IONPs at a low temperature can be attributed to the interaction between the magnetically soft IONP shell and relatively hard FePt core (**Figure S7**). In addition, hysteresis loops show that the initial susceptibility of cubic IONPs is higher than that of FePt@IONPs. The frequency dependent susceptibilities (Figure 3b) also reveal higher susceptibility for IONPs. It should be noted that the IONPs show a broader peak of the imaginary part of the susceptibility compared to FePt@IONPs. The fits of the susceptibility for polydisperse model of IONPs and monodisperse model of FePt@IONPs are presented in **Figure S8** [24-27], which indicate that the magnetic interaction between IONPs in solution is stronger than that between FePt@IONPs.

To further quantify the particle interaction of structurally uniform magnetite NPs [28, 29], we performed small-angle neutron scattering (SANS) at the NIST center for Neutron Research on beam lines NG3 and NG7. The nanocubic IONPs and FePt@IONPs were measured in a $D_2O$ solution at the concentration of 5mg/ml. The neutron scattering from $D_2O$ is similar to that of $Fe_3O_4$, thereby largely masking the structural scattering of the $Fe_3O_4$ while retaining its full magnetic scattering intensity. The cubic FePt@IONPs exhibit a $Q^{-2.5}$ Porod slope, as shown in Figure 3c, consistent with the presence of surfactant with a slope between that of mass fractal and surface fractal scattering [28, 29]. The cubic IONPs display the same Porod slope plus the addition of a shoulder which can be fitted using a cluster model of size 88 nm (or roughly 5-6

nanocubes). Given that the cubic FePt@IONPs exhibit no structural scattering features associated with the nanocube shape, the IONP cluster scattering appears to be magnetic in origin. The SANS data indicate that the IONPs tend to cluster together, while the FePt@IONPs nanocubes pack less tightly and do not exhibit aggregation when solvated. Consequently, the IONPs form inter-particle magnetic domains, while the magnetic domains of FePt@IONP nanocubes are limited in size to a single NP and exhibit no apparent magnetic coupling. Solvated IONPs consistently exhibit magnetic correlations, while FePt@IONPs do not. According to the SANS results, the primary function of the FePt is to disrupt the formation of the long-range magnetic dipolar interaction at zero field thereby reducing clustering in FePt@IONP.

Furthermore, using electron holography to observe interference fringe patterns allows a phase shift of the high-energy electron wave transmitted through the specimen to be measured by high-resolution TEM [30-32]. The electron holography of magnetic structures for FePt@IONPs and IONPs in dried samples demonstrates the natural magnetic vector fields within and between the particles, as shown in **Figure 4a** and 4b. The observed flux-closure domain of FePt@IONPs prevents the NPs from interacting with each other. The domain structure of nanocubes was simulated by using micromagnetic calculations (OOMMF code) [32], as shown in **Figure S9**. The magnetic induction flux lines in the two IONPs present an induction state characteristic of interacting nanocubes, but the flux closure state exhibited by the FePt@IONPs indicates a magnetic vortex configuration. The flux closure state of FePt@IONPs may explain a diversity of observations, including the suppressed long-range magnetic dipolar interaction in solution, susceptibility measurements and small-angle neutron scattering. The suppressed magnetic interaction in FePt@IONPs also helps prevent NP aggregation and cluster formation, consistent with our *in-vivo* observation that mice survival

rate is increased with FePt@IONPs due to the reduced detrimental effects on blood circulation.

During the MRI measurements, a strong magnetic DC field and a small orthogonal AC pulse field are applied, which may alter the NP configuration. To understand how the magnetic field influences the formation of magnetic clusters or assemblies, we deposited a solution containing NPs on a TEM grid. During the drying process, we applied magnetic fields. When a DC field of 0.47 T was applied, the IONPs yield bundles of IONP chains aligned with the DC field direction (Figure 4c). The long chains are broken down into separate small clusters by simultaneously applying an orthogonal AC pulse field of 0.5 mT at 20MHz and a DC field of 0.47T. The separated clusters are still aligned with the DC field (Figure 4d). On the other hand, the magnetically aligned FePt@IONP chains under a DC field (Figure 4e) are essentially unchanged by simultaneously applying AC pulse fields (Figure 4f). The evolutions of chains of IONPs and FePt@IONPs dispersed in water with a concentration of 0.5mM under DC and pulse AC fields applied were recorded in situ using an optical microscope and are shown in Supplementary Movie S1 and S2. The recording clearly demonstrates that the FePt cores seem to be strongly aligned by the DC field so that the FePt@IONPs chains cannot be dissociated with pulse AC fields. The effects of DC field on the assembly of IONPs and FePt@IONPs are also shown in **Figure S10**. When fields are off, both IONPs and FePt@IONPs chains are well dispersed again in the solution (Figure S10). Furthermore, the AC susceptibility spectra for both NPs in solution are unchanged after removing magnetic fields, which confirms the reversible assembly process from mono-dispersed NP (no field) to chains (in DC field) (**Figure S11**).

To understand how the interaction between NPs affects relaxation rate $R_2$ ($R_2=1/T_2$) in MRI measurement, we performed a Monte-Carlo simulation as described in ref. [19, 20] and methods. To compare experiments, we investigated the role of the local configuration by simulating the MRI of discontinuous chains for the IONP sample and continuous chains for the FePt@IONP sample. Each discontinuous or continuous (6×2×2) chain contains 24 particles. In addition, for comparison, we considered the case of single randomly-distributed particles. For each type of configuration, the system was constructed using approximately 1500 magnetic NPs. The relaxation rate as a function of concentration (packing density) for each configuration type is illustrated in **Figure 5a**. The $r_2$ relaxivity of the FePt@IONPs continuous chain is about 2.15 times higher than flocculated clusters of IONPs, which compares well to the experimental observation of 2.8 times (Figure 1a). The relaxation curves for the large structures (as experimentally illustrated in Figure 4) were also calculated to examine the role of the NP configurations at this scale (**Figure S12**).

The simulation corroborates the experimental data, showing the influence of spatial configuration on magnetic particle properties. Importantly it is demonstrated that the performance of magnetic NPs in MRI does not depend just on macroscopic properties such as packing density (average concentration), but also on microscopic properties (local concentration or local configuration/arrangement). The $R_2$ depends on the dipole field acting on each proton. This is non-uniform and strongly influenced by the geometry/position of the magnetic NPs as illustrated in Figure 5b and 5c. Here we show the dipole map of a section of the sample, which indicates the location and configuration of NPs. The dipole field map varies locally throughout the sample. This is supported by the dipole field histogram computed over the entire sample (Figure 5d), which highlights the influence of the NP configuration in enhancing the spatial distribution of dipolar fields. This has an important

effect on the MRI performance as the diffusing protons will experience different dipolar fields depending on the spatial location. If we analyze the tail of the dipole field distribution (related to large field and therefore fast dephasing, Figure 5e) we can see that there is a direct correlation of the distribution tail with the $R_2$ values. The NP chain has a systematically larger volume with a stronger dipole field compared to the discontinuous chains (discrete flocculated clusters). This corresponds to a faster dephasing of the protons and therefore an enhancement of the MRI performance (i.e. a larger $R_2$). As all the systems investigated here are identical, with the exception of the spatial configuration, we can conclude that the details of NP configuration have an important role to play in determining the MRI performance.

With the understanding of magnetic interaction effects on the relaxation and MRI contrast, we would like to further illustrate the uniqueness of our core-shell structures. The presence of superparamagnetic FePt core plays an important role on the magnetic interaction among NPs. At zero field, the existence of a FePt core leads to the formation of closure domains within FePt@IONPs, which disrupts the formation of the long-range dipolar interaction. The energy cost of forming a vortex is the exchange energy associated with a point-divergence of the magnetization at the center. Applying a field stabilizes the magnetization of FePt and makes the vortex structure less energetically feasible, leading to the observed chain formation in an applied field. The reduced dipolar interaction in zero field helps the circulation of NPs in the bloodstream and enhances SAR. On the other hand, under a strong DC field, the FePt core is strongly aligned by the DC field such that the NPs chains are not disturbed by the applied AC pulse field. The chain configuration formed by magnetic fields reveals a stronger dipolar field around the chain, which corresponds to a faster dephasing of the proton and therefore an enhancement of the MRI performance. We would like to emphasize that our approach can be combined with other methods to further increase relaxivity. For example, by increasing the particle size (17.8 nm) of superparamagnetic core-shell structure, we can further improve the

relaxivity to 411.3 $mM^{-1}s^{-1}$, as shown in Figure S13. Our approach shows great potential to reach even higher $r_2$ by further optimization. Thus, highly effective multifunctional NPs for bio-applications can be successfully realized by designing core-shell structures to tune magnetic interactions among NPs.

For hyperthermia treatment, cubic NPs have been reported to have a higher SAR than spherical ones due to increased anisotropy [33]. The magnetic core-shell structure with exchange coupling between a magnetically hard core and soft shell can further enhance anisotropy and thus the SAR [14]. In addition to anisotropy, the simulations reveal that reduced magnetic dipolar interaction among NPs can raise the SAR [34]. Both susceptibility spectra (Figure 3b) and small-angle neutron scattering spectra (Figure 3c) show that the FePt@IONP suspension has greatly reduced magnetic dipolar interactions between NPs in zero field compared to IONPs, which may also contribute to the enhanced SAR.

In summary, this report demonstrates that superparamagnetic cube FePt@IONPs core-shell NPs are suitable to be used as theranostic agents because of their higher relaxivity and SAR value. We reveal that the magnetic NP interaction not only influences the $T_2$ weighted image but also the SAR. The FePt core is essential for forming the specific flux-closure domain in the core-shell structure. The cubic FePt@IONP core-shell has several prominent advantages. Firstly, the magnetic core-shell structure, with lower magnetic dipole-dipole interactions among the particles, can be designed to stabilize magnetic NPs against aggregation caused by magnetic interactions in the remanent state. Secondly, the FePt core may be exchange-coupled to the IONP shell, which significantly enhances the SAR. Furthermore, the presence of the FePt core maintains chain-like assemblies during AC field pulses in MRI measurement, which essentially enhances $R_2$. With the ability to tune magnetic interactions between NPs,

the design of multifunctional cubic FePt@IONP can be devoted to improving the resolution of the MRI image and effective hyperthermia for theranostic applications.

**Experimental Section**

***Synthesis of FePt cores:*** Synthesis of FePt NPs was carried out by using standard Schlenk line techniques under Ar atmosphere. In a typical synthesis process, $Pt(acac)_3$ (0.25 mmol), $Fe(CO)_5$ (0.75 mmol), 1,2-hexadecanediol (2 mmol), oleic acid (1.2 mmol), and oleylamine (1.2 mmol) were mixed and dissolved in benzyl ether (10 mL). The mixed solution was heated to 290°C with a heating rate of 5°C/min. The temperature was kept at 290°C for 30 min. Then the solution was naturally cooled to room temperature. The NPs were washed by ethanol and redispersed in hexane several times. The final product was stored in hexane.

***Synthesis of cubic $Fe_3O_4$ and FePt@IONP:*** The details of synthesis of cubic $Fe_3O_4$ can be found in ref. [35] and the similar approach was used for the synthesis of the shell of FePt@IONPs. The synthesis of the shaped FePt@IONP core/shell nanocubes involved two steps, including the synthesis of a FePt core and the overgrowth of a shaped $Fe_3O_4$ shell. The prepared FePt NPs were mixed with oleic acid (0.3 mmol), oleylamine (0.3 mmol), and 1, 2-tetradecanediol (5 mmol) and were dissolved in benzyl ether (15 mL) which served as the reaction solution. For the precursor solution, $Fe(acac)_3$ (1 mmol) was dissolved in benzyl ether (5 mL). The reaction solution was dewatered at 120°C for 1 hour and was then heated to the reflux temperature of 290°C. Then, the precursor solution was injected into the hot reaction solution at 290°C with an injection rate of 10 mL/h. The fluctuation of the reaction temperature was less than 5°C during the injection process. After the reaction was finished, the NPs were washed in ethanol and redispersed in hexane. Both $Fe_3O_4$ NPs and FePt@IONP were modified with short-chain surfactants (such as CTAB or mPEG) to be dispersed in water.

***Synthesis of CTAB-FePt@IONP:*** The core-shell FePt@IONP were then dried under vacuum and added into an aqueous solution containing 0.1 M CTAB (FW: 364.45). After 10 min

sonication, the core-shell FePt@IONP NPs were coated by CATB and formed stable NP dispersion in water.

***Synthesis of mPEG-FePt@IONP:*** We use the dopamine-based surfactant to replace oleylamine around the iron oxide nanoparticles as reported in ref. [36]. To functionalize the FePt@IONP nanoparticles with mPEG, Trichloro-*s*-triazine (TsT) (22 mg) was first used to react with mPEG (average mol wt: 350) (200mg) at room temperature in anhydrous benzene (20 mL) to form TsT-mPEG. Then, TsT-mPEG (20mg) reacts with dopamine hydrochloride (20 mg) in 1,4-dioxane solvent, forming compound. The catecol unit in dopamine-based molecule is used to replace oleylamine around the iron oxide NPs, forming stable NP dispersions in water.

**Acknowledgements**
This work was partially supported by the Ministry of Science and Technology of Republic of China under Grant No. NSC 102-2221-E-007-043-MY2 and Technology Development Program for Academia (H301ARY431). Fu-Rong Chen thank for the support from the project NSC 96-2628-E-007-017-MY3 and NSC 101-2120-M-007-012-CC1. And this work made use of the facilities of N8 HPC provided and funded by the N8 consortium and EPSRC (Grant No. EP/K000225/1) coordinated by the Universities of Leeds and Manchester and the EPSRC Small items of research equipment at the University of York ENERGY (Grant No. EP/K031589/1). All the animals received care in accordance with the Guidance Suggestions for the Care and Use of Laboratory Animals. The procedures were approved by the Institutional Animal Care and Use Committee of National Chung Hsing University (IACUC of NCHU).

Received: ((will be filled in by the editorial staff))
Revised: ((will be filled in by the editorial staff))
Published online: ((will be filled in by the editorial staff))

References

[1] I. Hilger, W. A Kaiser, *Nanomedicine* **2012**, 7, 1443.

[2] A. Hervault, N. T. K. Thanh, *Nanoscale* **2014**, 6, 11553.

[3] S. Dutz, R. Hergt, *Int. J. of Hyperthermia* **2013**, 29, 790.

[4] J. Xie, S. Lee, X. Chen, *Adv. Drug. Deliv. Rev.* **2010**, 62, 1064.

[5] U. I. Tromsdorf, N. C. Bigall, M. G. Kaul, O. T. Bruns, M. S. Nikolic, B. Mollwitz, R.

A. Sperling, R. Reimer, H. Hohenberg, W. J. Parak, S. Förster, U. Beisiegel, G. Adam, H. Weller, *Nano Lett.* **2007**, 7, 2422.

[6] J. H. Lee, Y. M. Huh, Y. W. Jun, J. W. Seo, J. T. Jang, H. T. Song,S. Kim, E. J. Cho, H. G. Yoon, J. S. Suh, J. W. Cheon, *Nat. Med.* **2007**, 13, 95.

[7] Y. W. Jun, Y. M. Huh, J. S. Choi, J. H. Lee, H. T. Song, S. Kim, S. Yoon, K. S. Kim, J. S. Shin, J. S. Suh, J. W. Cheon, *J. Am. Chem. Soc.* **2005**, 127, 5732.

[8] E. Pöselt, H. Kloust, U. Tromsdorf, M. Janschel, C. Hahn, C. Maßlo, H. Weller, *ACS Nano* **2012**, 6, 1619.

[9] T. J. Yoon, H. Lee, H. Shao, S. A. Hilderbrand, R. Weissleder, *Adv. Mater.* **2011**, 23, 4793.

[10] S. Tong, S. Hou, Z. Zheng, J. Zhou, G. Bao, *Nano Lett.* **2010**, 10, 4607.

[11] C. Paquet, H. W. de Haan, D. M. Leek, H. Y. Lin, B. Xiang, G. Tian, A. Kell, B. Simard, *ACS Nano* **2011**, 5, 3104.

[12] J. M. Perez, L. Josephson, T. O'Loughlin, D. Högemann, R. Weissleder, *Nat. Biotechnol.* **2002**, 20, 816.

[13] P. Qiu, C. Jensen, N. Charity, R. Towner, C. Mao, *J. Am. Chem. Soc.* **2010**, 132, 17724.

[14] J. H. Lee, J.T. Jang, J. S. Choi, S. H. Moon, S. H. Noh, J. W. Kim, J. G. Kim, I. S. Kim, K. I. Park, J. W. Cheon, *Nat. Nanotechnol.* **2011**, 6. 418.

[15] S. H. Noh, W. Na, J. T. Jang, J. H. Lee, E. J. Lee, S. H. Moon, Y. Lim, J. S. Shin, J. W. Cheon, *Nano Lett.* **2012**, 12, 3716.

[16] J. Gao, G. Liang, J. S. Cheung, Y. Pan, Y. Kuang, F. Zhao, B. Zhang, X. Zhang, E. X. Wu, B. Xu, *J. Am. Chem. Soc.* **2008**, 130, 11828.

[17] H. Khurshid, C. G. Hadjipanayis, H. Chen, W. Li, H. Mao, R. Machaidze, V. Tzitzios , G. C. Hadjipanayis, *J. Magn. Magn. Mater.* **2013**, 331, 17.

[18] Z. Zhao1, Z. Zhou, J. Bao, Z. Wang, J. Hu, X. Chi, K. Ni, R. Wang, X. Chen, Z. Chen, J. Gao, *Nat. Comms.* **201**3, 13, 95.

[19] O. L. Gobbo, K. Sjaastad, M. W. Radomski, Y. Volkov, A. Prina-Mello, *Theranostics* **2015**, 5, 1249.

[20] C Klifa, S Suzuki, S Aliu, L Singer, L Wilmes, D Newitt, B Joe, N Hylton, *J Magn Reson Imaging* **2011**, 33, 1229.

[21] M.A. Al-Nasassrah, F. Podczeck, J.M. Newton, *Euro. J. Pharm. Biopharm*. **1998**, 46, 31.

[22] H. W. de Haan, *Magn. Reson. Med.* **2011**, 66, 1748.

[23] R. A. Brooks, F. Moiny, P. Gillis, *Magn. Reson. Med.* **2001**, 45, 1014.

[24] D. Eberbeck, F. Wiekhorst, U. Steinhoff, L. Trahms, *J. Phys.: Condens. Matter.* **2006**, 18, S2829.

[25] V. Singh, V. Banerjee, M. Sharma, *J. Phys. D: Appl. Phys.* **2009**, 42, 245006.

[26] P. C. Fannint, S. W. Charles, *J. Phys. D: Appl. Phys.* **1989**, 22, 187.

[27] J. P. Fortin, C. Wilhelm, J. Servais, C. Ménager, J. C. Bacri, F. Gazeau, *J. Am. Chem. Soc.* **2007**, 129, 2628.

[28] B. Hammouda, D. L. Ho, S. R. Kline, *Macromolecules* **2004**, 37, 6932.

[29] K. L. Krycka, R. A. Booth, C. R. Hogg, Y. Ijiri, J. A. Borchers, W. C. Chen, S. M. Watson, M. Laver, T. R. Gentile, L. R. Dedon, S. Harris, J. J. Rhyne, S. A. Majetich, *Phy. Rev. Lett.* **2010**, 104, 207203

[30] J. M. THOMAS, E. T. SIMPSON, T. KASAMA, R. E. DUNIN-BORKOWSKI, *Acc. Chem. Res.* **2008**, 41, 665.

[31] E. Snoeck, C. Gatel, L. M. Lacroix, T. Blon, S. Lachaize, J. Carrey, and M. Respaud, B. Chaudret, *Nano Lett.* **2008**, 8, 4293.

[32] L. M. Lacroix, S. Lachaize, F. Hue, C. Gatel, T. Blon, R. P. Tan, J. Carrey, B. Warot-Fonrose, B. Chaudret, *Nano Lett*. **2012**, 12, 3245.

[33] C. Martinez-Boubeta, K. Simeonidis, A. Makridis, M. Angelakeris, O. Iglesias, P. Guardia, A. Cabot, L. Yedra, S. Estradé, F. Peiró, Z. Saghi, P. A. Midgley, I. Conde-Leborán, D. Serantes, D. Baldomir, *Sci Rep.* **2013**, 3, 1652.

[34] L. C. Branquinho, M. S. Carrião, A. S. Costa, N. Zufelato, M. H. Sousa, R. Miotto, R. Ivkov, A. F. Bakuzis, *Sci Rep.* **2013**, 3, 2887.

[35] C. H. Ho, C. P. Tsai, C. C. Chung, C.-Y. Tsai, F. R. Chen, H. J. Lin, C. H. Lai, *Chem. Mater.* **2011**, 23, 1753.

[36] J. Xie, C. Xu, Z. Xu, Y. Hou, K. L. Young, S. X. Wang, N. Pourmand, S. Sun, *Chem. Mater.* **2006**, 18, 5401.

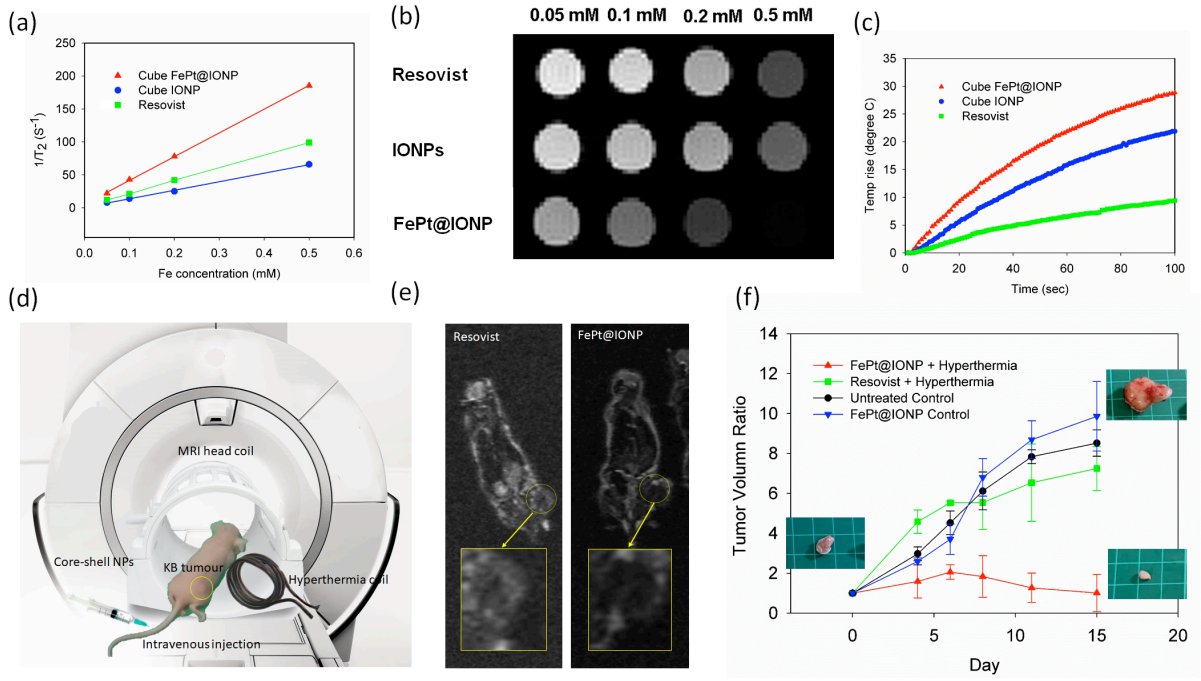


**Figure 1. (a)-(c) The relaxivity and hyperthermia measurement of NPs.** (a) The variation of $1/T_2$ with Fe concentration of cubic FePt@IONPs (red triangle line), Resovist® (green square line) and cubic IONPs (blue circle line) measured at 4.7 T. The $r_2$ relaxivities ($mM^{-1}s^{-1}$) were obtained from fitting the slope of each sample. (b) $T_2$-weighted images of Resovist®, cubic IONPs, and cubic FePt@IONPs with the same Fe concentration, measured at 4.7T. (c) Measurement of heat generation of the NPs, carried out by using an AC magnetic field produced from radiofrequency heating machine. The rate of the temperature increase was 0.29℃/s, 0.22℃/s and 0.04℃/s for FePt@IONP, IONP and Resovist®, respectively. **(d)-(f) *In vivo* thernanostic performance of NPs** (d) schematic picture shows real-time MRI-controlled magnetic hyperthermia system for tumor treatment (e) T2*-weighted MR images of KB tumor of a mouse with Resovist® (left) and FePt@IONP (right). (f) Plot of tumor volume ratio (tumor volume/initial tumor volume) versus days after treatment with FePt@IONP hyperthermia, Resovist® hyperthermia, untreated control and FePt@IONP control.

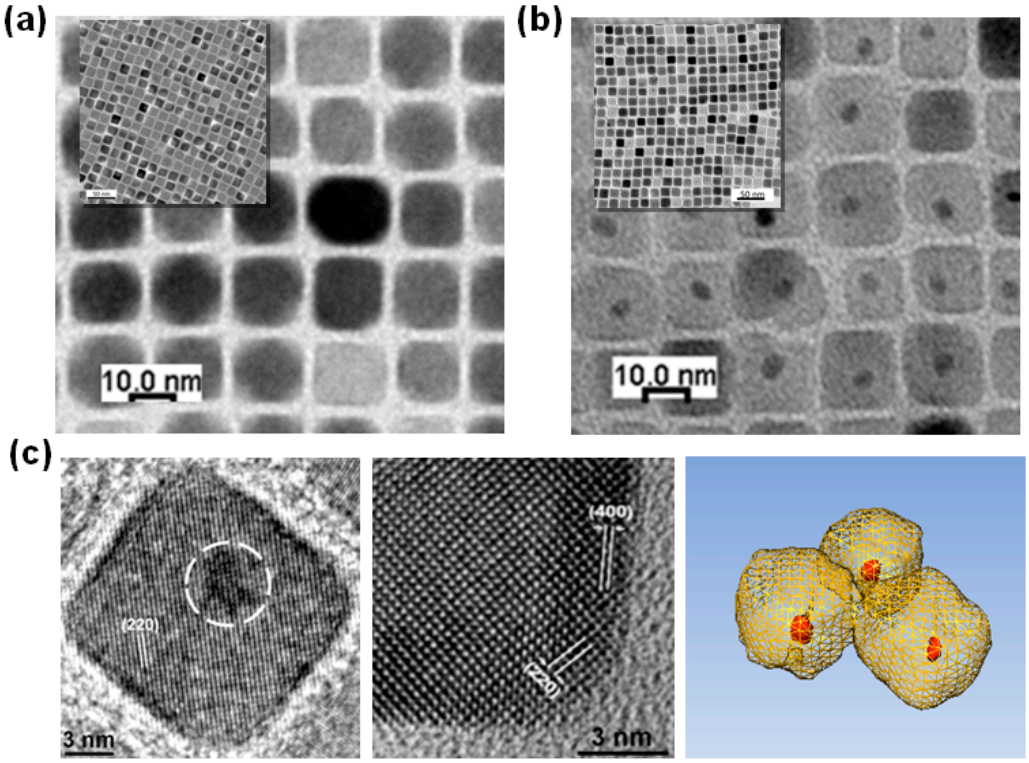


**Figure 2. Structural and microstructural analyses of IONPs and FePt@IONPs.** (a) The TEM image of cubic IONPs. (b) The TEM image of cubic FePt@IONPs. The core-shell NPs with FePt core and $Fe_3O_4$ cubic shell are further demonstrated by (c) (left) the HRTEM images (The dashed circle indicates the position of FePt core). (mid) The lattice fringes correspond to {220} lattice planes of IONPs while the facet is {100}. (right) The 3D TEM tomography of FePt@IONPs core-shell structure.

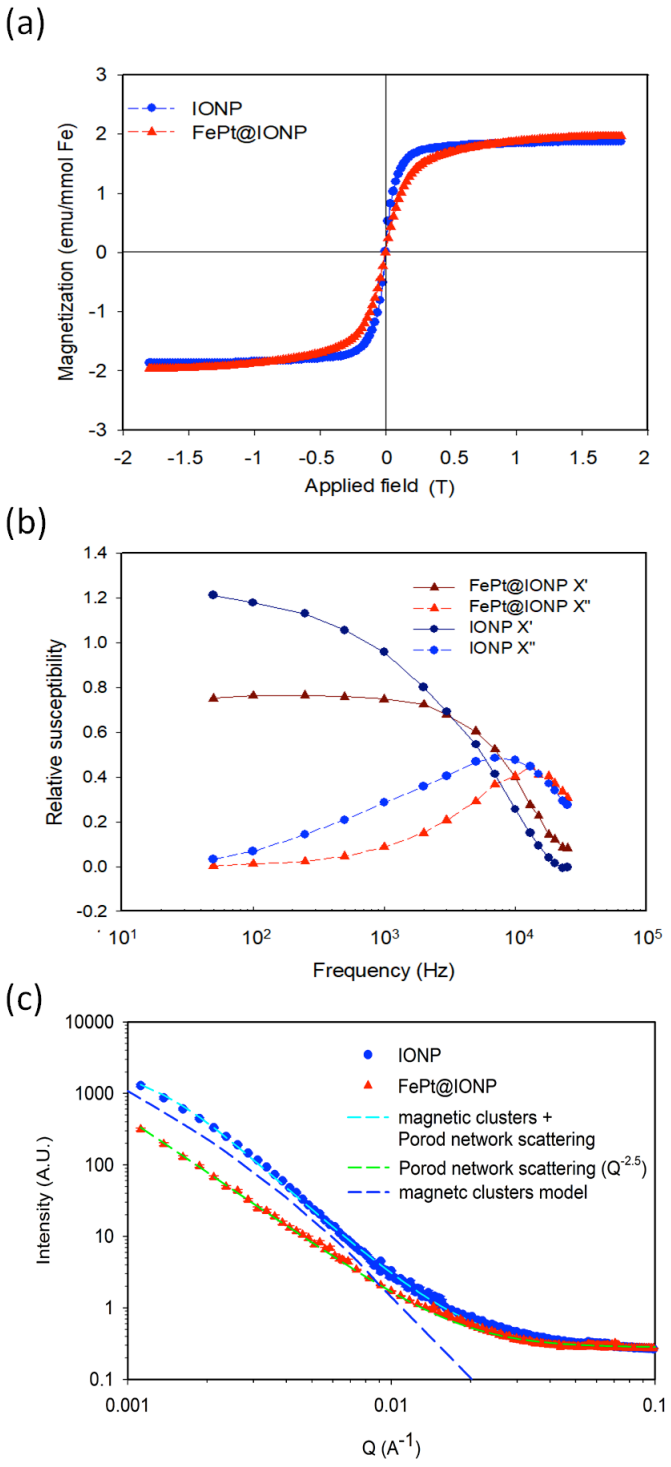


**Figure 3. Magnetic properties and magnetic structural scattering of NPs** (a) Magnetic hysteresis loops of FePt@IONPs and IONPs dispersed in water with the concentration of 1mgFe/ml. (b) The real and imaginary parts of magnetic susceptibility frequency spectra of FePt@IONPs and IONPs dispersed in water with the concentration of 1mgFe/ml. (c) Small-angle neutron scattering fitted by the Porod network scattering and magnetic clusters model. Solvated cubic IONPs (blue circle line) reveal long-range magnetic scattering that is absent in cubic FePt@IONPs (red triangle line).

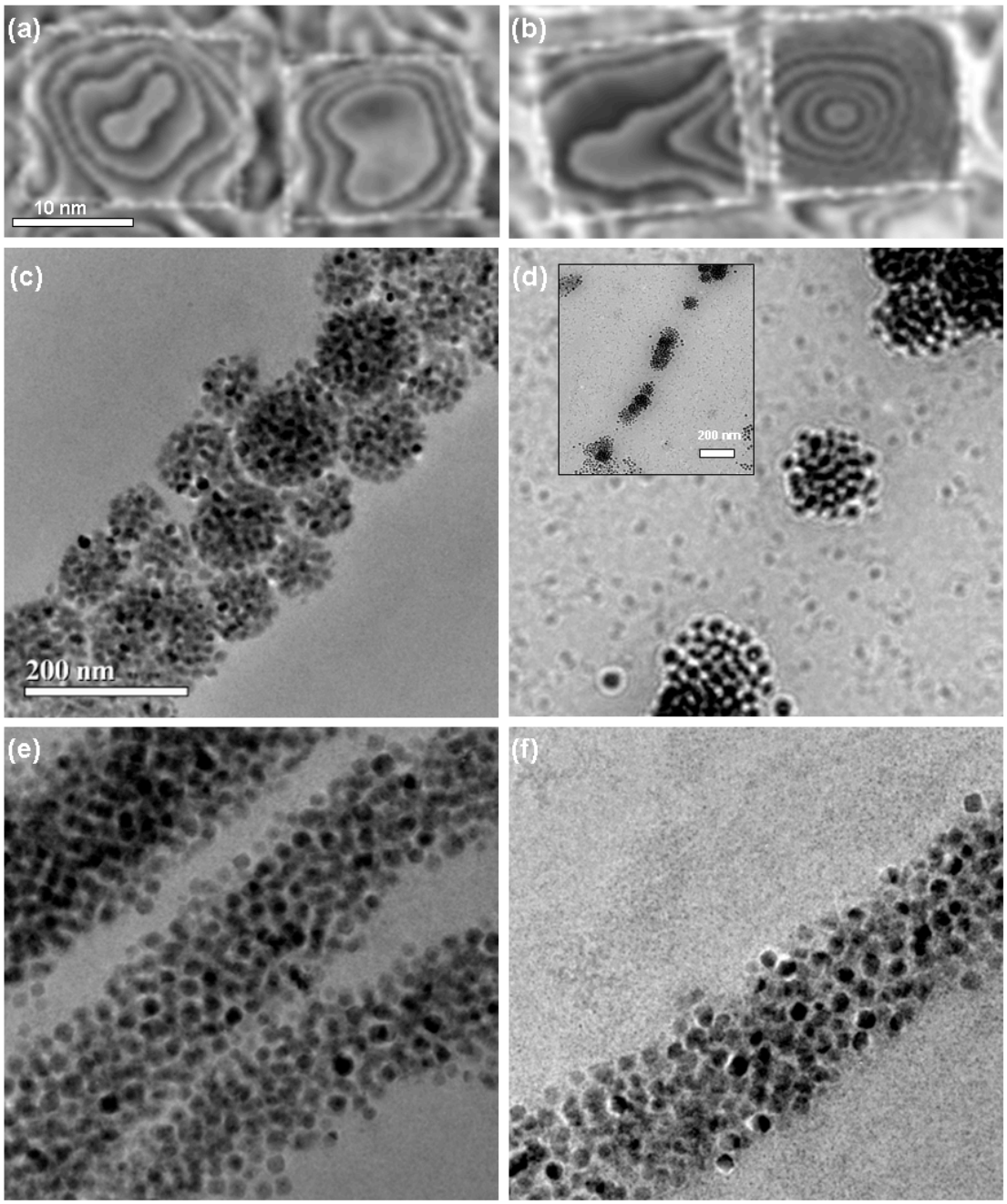


**Figure 4. Electron holography and TEM analyses of NPs** The magnetic induction maps recorded using off-axis electron holography at the remanent state for (a) cubic FePt@IONPs and (b) cubic IONPs (the white dotted-lines are added to indicate the location of NPs). (c)-(f) show TEM images, and the inset in (d) show a large scale image, for NPs with a Fe concentration of 0.5 mM. (c) IONPs under a DC magnetic field of 0.47T and (d) IONPs under the DC magnetic field of 0.47T and an orthogonal AC field of 0.5 mT at 20MHz. (e) FePt@IONPs under a DC magnetic field of 0.47T and (f) FePt@IONPs under a DC magnetic field of 0.47T and an orthogonal AC field of 0.5 mT at 20MHz.

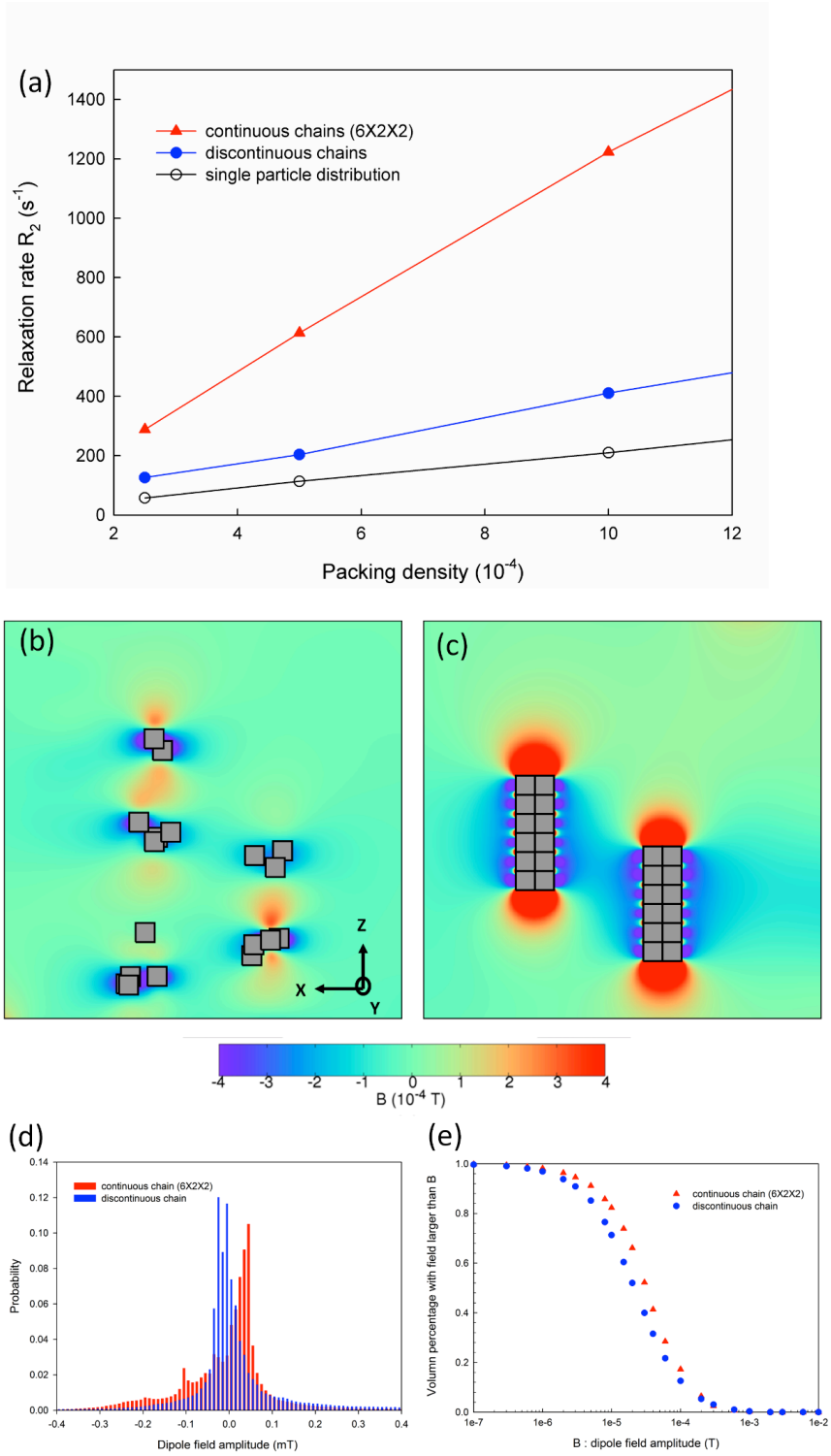


**Figure 5. $R_2$ results from Monte Carlo simulation.** (a)The dependence of $R_2$ on the packing density for two configurations of NPs: the continuous chains (red triangle) and the aligned discrete clusters (discontinuous chain: blue circle). For reference we also consider the case where the NPs are separated (single particle: open circle). Colour map of the dipole field in a system of: (b) discontinuous chains (X-Z plane) and (c) continuous chains (6X2X2). The number of particle per cluster for discontinuous chains is 6 in the 3D structure. (d) Statistics of the dipole field amplitude for continuous and discontinuous chains. (e) Statistics of volume percentage with field larger than a given value. This corresponds to the tail of the dipole field distribution in the sample volume, which is responsible for the fast dephasing. The continuous chain has a larger field overall, leading to a larger $R_2$.

**Keyword**: magnetic resonance image, hyperthermia, theranostics, core-sell, magnetic interaction

Ming-Da Yang, Chien-Hsin Ho, Sergiu Ruta, Roy Chantrell, Kathryn Krycka, Ondrej Hovorka, Fu-Rong Chen, Ping-Shan Lai, and Chih-Huang Lai*

**Title**: **Magnetic interaction of multifunctional core-shell nanoparticles for highly effective theranostics**

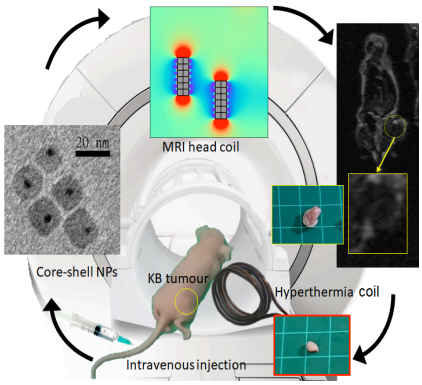


ToC figure (size: 55 mm broad × 50 mm high)

We demonstrate that magnetic interaction among nanoparticles can be manipulated by core-shell structure to enhance the resolution of magnetic resonance image (MRI) and specific absorption rate of nanoparticles. It is rather remarkable that we can control the magnetic configuration of assembly shape under magnetic field to improve relaxivity of contrast agent and effectiveness of hyperthermia, making theranostics feasible.

# Supporting Information

**Magnetic interaction of multifunctional core-shell nanoparticles for highly effective theranostics**

*Ming-Da Yang, Chien-Hsin Ho, Sergiu Ruta, Roy Chantrell, Kathryn Krycka, Ondrej Hovorka, Fu-Rong Chen, Ping-Shan Lai, and Chih-Huang Lai**

S1: SAR calculations of IONPs and FePt@IONPs.

The experimental setup for magnetically induced hyperthermia included a copper coil cooled with circulating water, and a resonant RLC circuit producing an AC magnetic field up to 18.8 kA/m at 630 kHz, which could increase the temperature of magnetic nanoparticles in water. By using the optical fiber thermometer to probe temperature in the center of the sample, the specific absorption rate (SAR) of superparamagnetic material is deduced from the initial linear rise of the plot of temperature versus time, $\Delta T/\Delta t$ (Figure 1c in the manuscript) and the heat capacity of the sample, normalized to the mass of magnetic material. The nanoparticle concentration in water was 1 mg/ml. SAR can be expressed as Equation S1 [1, 2, 3]:

$$SAR = C\frac{\Delta T}{\Delta t} \quad \text{(S1)}$$

where C is the volumetric specific heat capacity of water, 4185 J/(kg・K). From the experimental data, commercially available $Fe_3O_4$ nanoparticles (Resovist) and our cubic IONPs show SAR values of 0.39 kW/g and 0.92 kW/g, respectively, while FePt@IONPs exhibits a value of 1.21 kW/g.

S2: T2*-weighted MR images of FePt@IONPs.

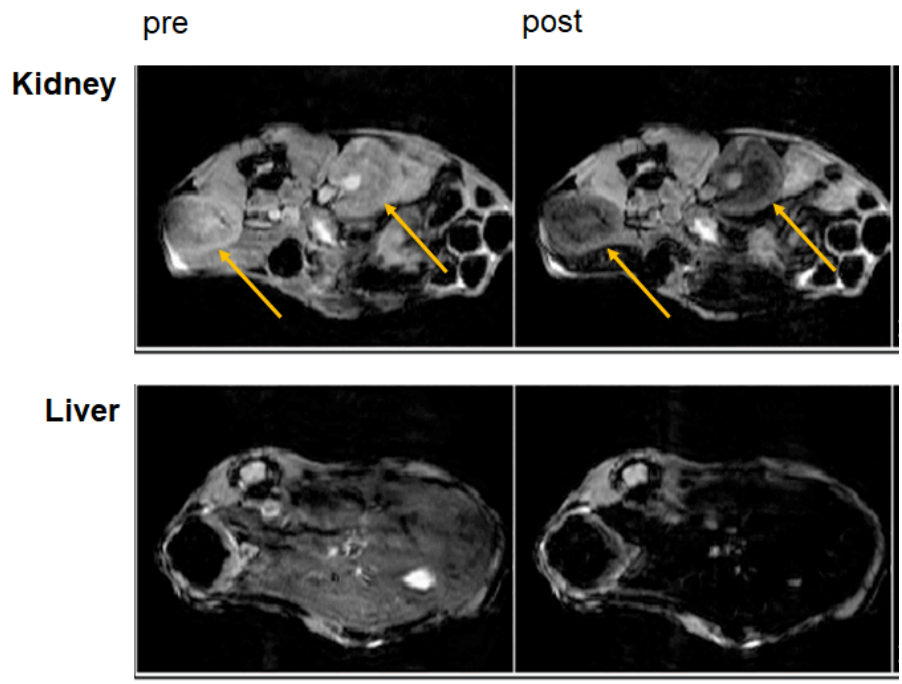


Figure S1. MR images for kidney and Liver of mice before and after intravenous injection of FePt@IONP.

The images with a body-adapted mould demonstrate a significantly improved MRI contrast in the kidneys and livers of mice between Pre- and Post-injection (shown in Figure S1).

S3: Structural analyses of IONPs and FePt@IONPs.

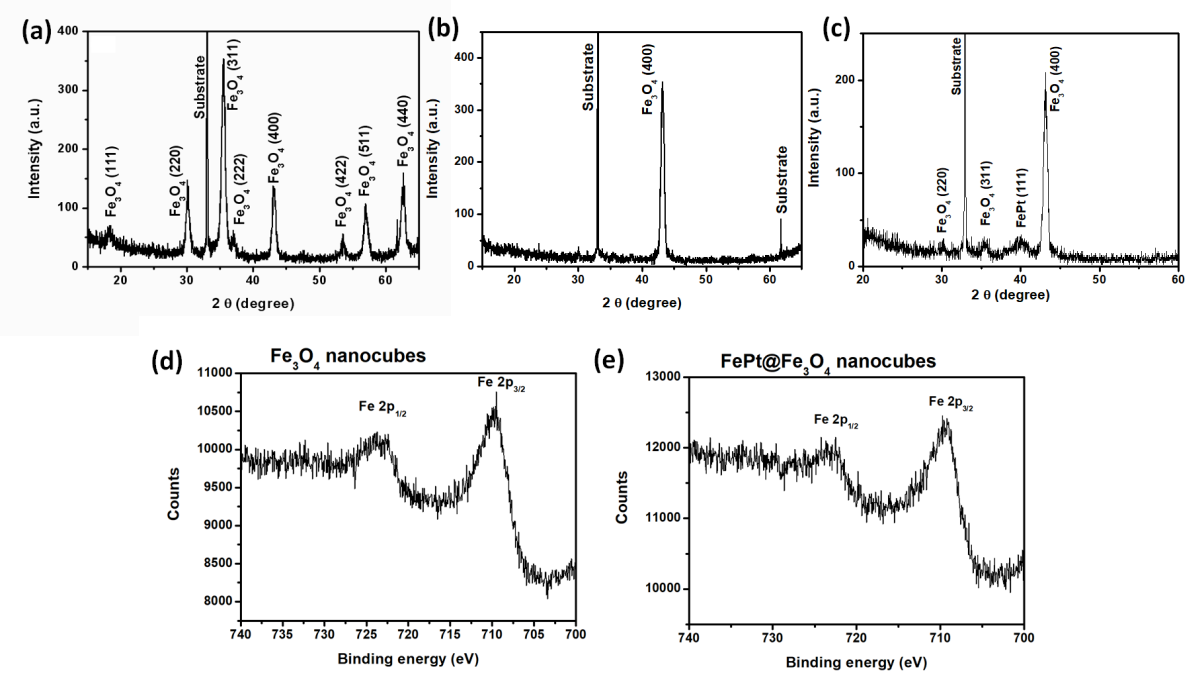


**Figure S2**. The XRD data of (a) IONPs with randomly packed, (b) IONPs with cube surface parallel to the substrate and (c) FePt@IONPs with cube surface parallel to the substrate, X-ray photoelectron spectrum (XPS) of (d) $Fe_3O_4$ nanocubes, and (e) FePt@$Fe_3O_4$ nanocubes

X-ray diffraction (XRD) patterns were detected by using Shimadzu XRD 6000 with Cu Kα radiation. The XRD samples were prepared by dropping the nanoparticle dispersion on Si substrates with a controlled solvent evaporating rate. After the solvent was evaporated, the dried nanoparticles on Si substrates were used for XRD measurement. With the varied evaporation rate of solvent, the nanocubes can be either randomly packed, or packed with the cube surface parallel to the substrate, that is, (400)-preferred orientations. The XRD data of IONPs with randomly packed (a), IONPs with cube surface parallel to the substrate (b) and FePt@IONP with cube surface parallel to the substrate (c) are shown in **Figure S2**. The XPS measurements were collected using synchrotron-based light source at the National Synchrotron Radiation Research Center (NSRRC) in Hsinchu, Taiwan. This method was chosen because synchrotron radiation provides high-intensity light of well-defined characteristics with a continuous spectrum ranging from infrared to X-ray. No satellite peaks

between the peaks of Fe $2p_{3/2}$ and Fe $2p_{1/2}$ were observed for $Fe_3O_4$ and FePt@$Fe_3O_4$ nanocubes, as shown in Figure S2 (d) and (e), indicating that these nanocubes were consistent with the $Fe_3O_4$ component.

S4: Surfactant effect on the $r_2$ and SAR of FePt@IONP NPs

(a) (b)

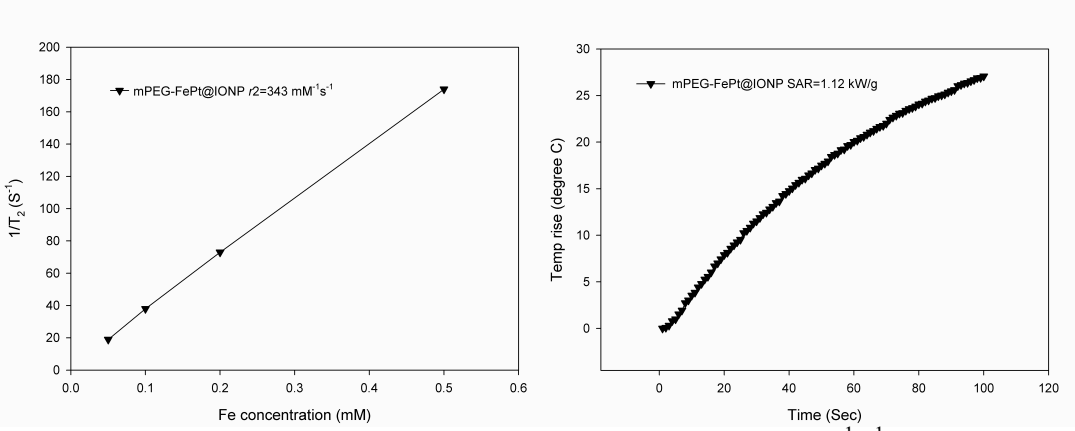


Figure S3 (a) The $r_2$ relaxivity of mPEG-FePt@IONP is 343 $mM^{-1}s^{-1}$. (b) The rates of temperature increase is 0.268℃/s for mPEG-FePt@IONP.

To improve bio-compatability of NPs, we change the surfactant CTAB to mPEG. The reuslts shown in Figure S3 reveal that no significant difference between CTAB and mPEG coated FePt@IONPs on the enhancement of MRI ($r_2$) and hyperthermia (SAR). The $r_2$ relaxivities of CTAB-FePt@IONP and mPEG-FePt@IONP are 360 and 343 $mM^{-1}s^{-1}$, respectively. The rates of temperature increase are 0.290℃/s and 0.268℃/s for CTAB-FePt@IONP and mPEG-FePt@IONP, respectively. The corresponding SAR values are 1.21 KW/g and 1.12 KW/g, respectively.

S5: Cytotoxicity evaluation of FePt@IONP NPs

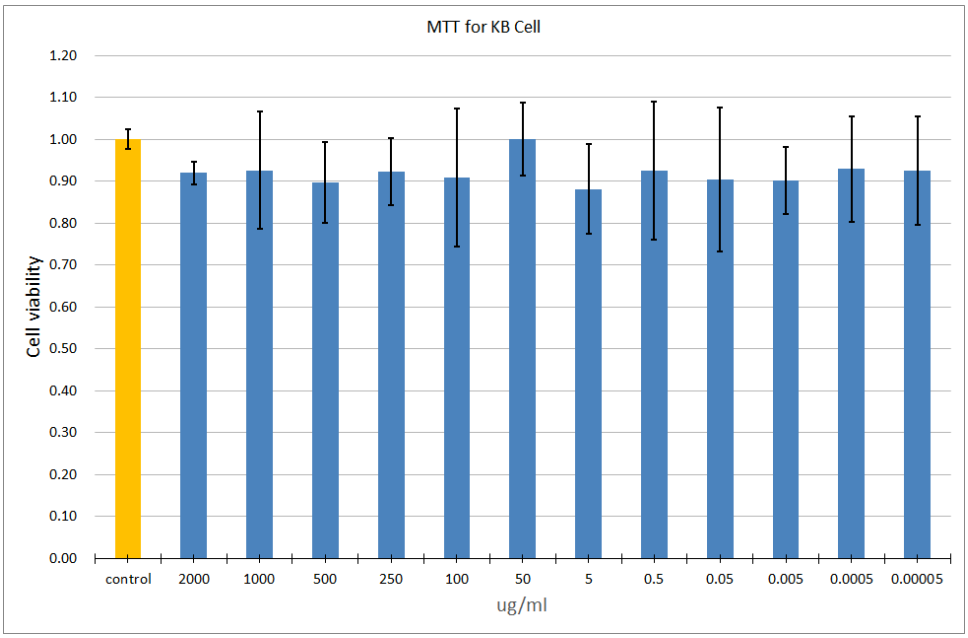


Figure S4. Effect of different concentration of mPEG-coated FePt@IONPs on cell viability

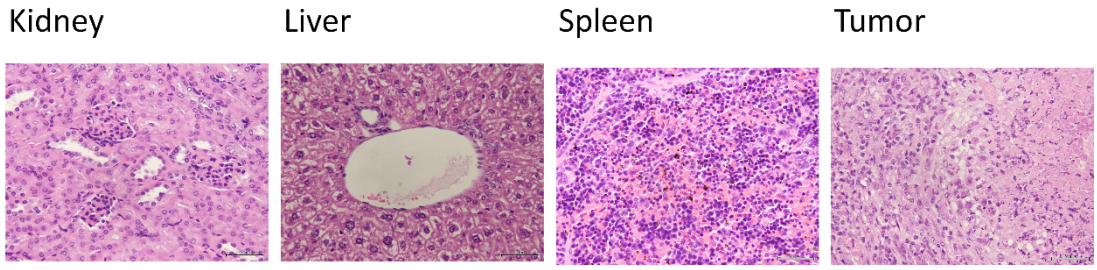


Figure S5. H&E staining of major organs after the magnetic hyperthermia treatment with FePt@IONP NPs.

Cell viability was assessed by using the MTT assay, which was based on the reduction of the dye MTT to formazan crystals, an insoluble intracellular blue product, by cellular dehydrogenases. MTT assays show that the mPEG-coated FePt@IONPs have no toxic reaction for KB cells, as shown in Figure S4. Furthermore, after magnetic hyperthermia treatment, we performed H&E staining, which reveals that normal cells are still live in the major organs but magnetic hyperthermia leads to apoptosis and necrosis in tumor tissue, shown in Figure S5. This result also confirms no cytotoxicity issue for FePt@IONP NPs.

S6: Stability of FePt@IONP NPs

(a) (b)

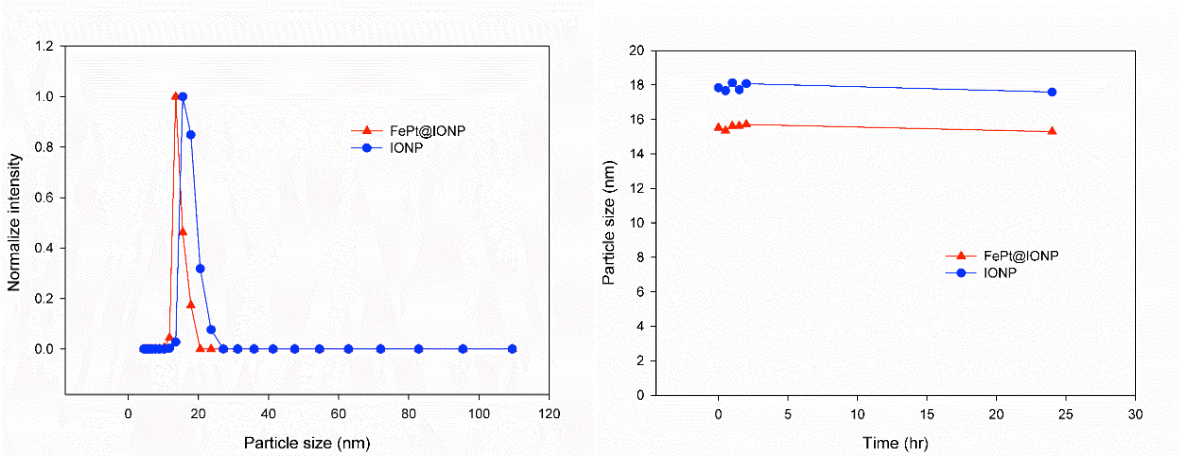


Figure S6 (a) Particle size distribution of FePt@IONP and IONP. (b) Variations of particle size with time.

Dynamic light scattering (DLS) is a well-known technique used for studying the stability of NPs. The DLS results reveal that the mean size of FePt@IONP is 15.5 nm and the size of NPs ranges from 11.7 to 20.5 nm (Figure S6a). The mean size and range of IONPs are slightly larger than those of FePt@IONP. No significant changes of mean size of both FePt@IONP and IONPs for 24 hrs, observed by DLS, indicating good stability of FePt@IONP and IONPs without aggregation (Figure S6b).

S7: Exchange-coupled properties of FePt@IONPs.

(a) (b)

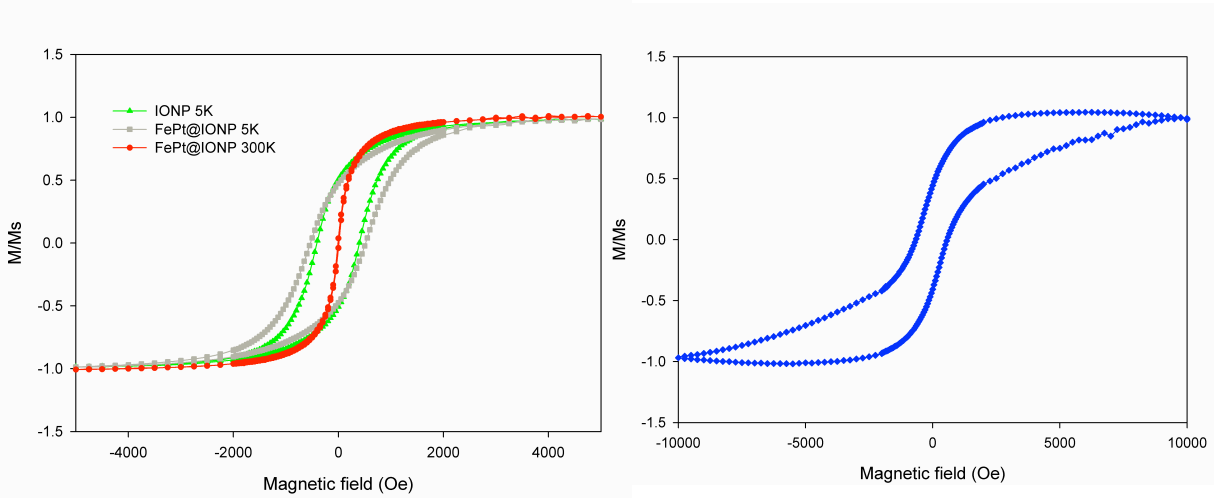


**Figure S7**. Exchange-coupled properties of core-shell FePt@IONPs were investigated by using M-H curve measurements with a superconducting quantum interference device (SQUID). (a) M-H curve of FePt@IONP at 300K and 5 K and M-H curve of IONP at 5 K . (b) M-H curve of FePt nanoparticles at 5 K. The red curve shows its superparamagnetic nature with zero coercivity at 300K. FePt@IONPs (grey curve) show larger coercevity than IONPs (green curve) at 5 K.

Since all nanoparticles are superparamagnetic at room temperature, to get information of exchange coupling between core and shell, we measure the hysteresis loops at 5K, shown in **Figure. S7a**. The disordered FePt core reveals a larger coercivity than IONPs and FePt@IONPs, shown in the inset of Figure S7b. Since the volume ratio of FePt core is only 1% of core-shell nanoparticles, the increased coercivity of FePt@IONPs compared to IONPs can be attributed to the presence of exchange coupling between soft $Fe_3O_4$ shell and relatively hard FePt core [4,5]

S 8: The fitting of the Imaginary susceptibility for IONPs and FePt@IONPs

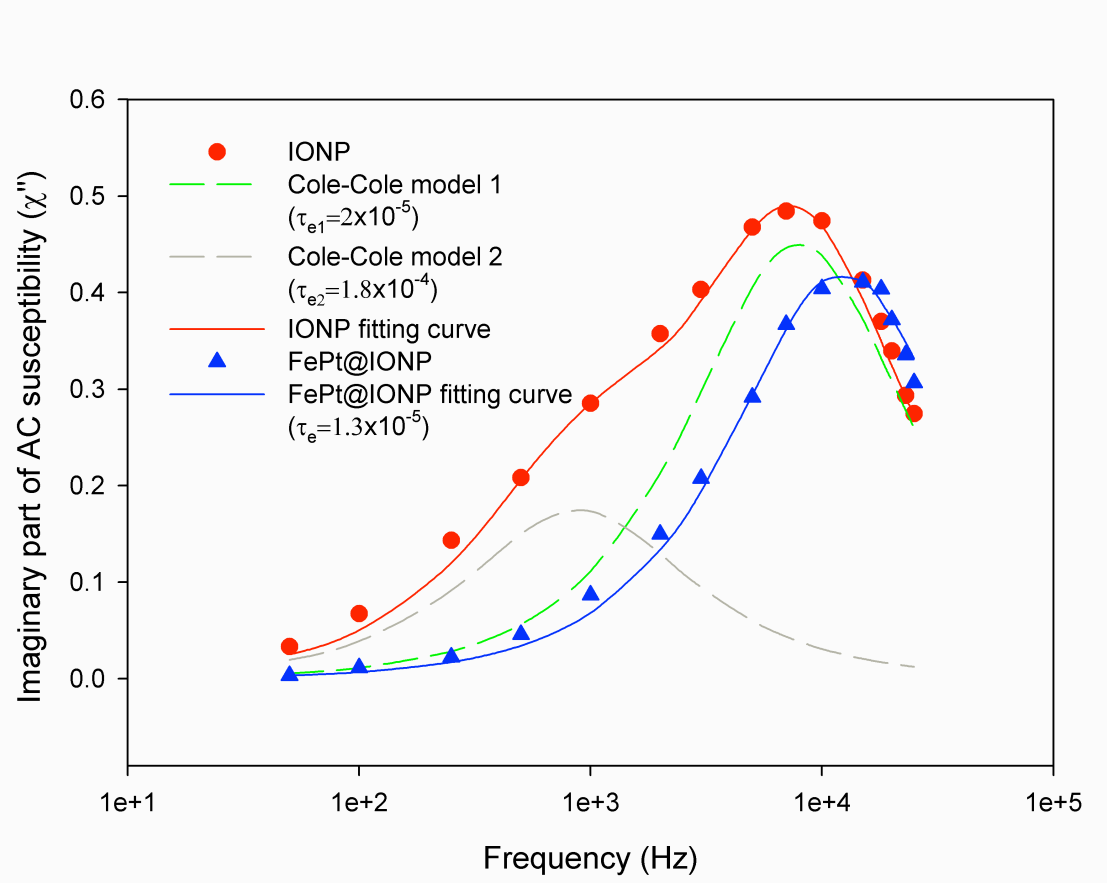


**Figure S8**. Imaginary susceptibility as function of frequency for IONP (red circle) and FePt@IONP (blue triangle). Using the Cole-Cole model with two symmetric peaks (gray and green dash line), we can fit the AC susceptibility curve of IONPs. Only one symmetric peak is needed to fit the AC susceptibility curve of FePt@IONP.

The information on interaction behavior can be obtained from AC susceptibility measurements $\chi''(\omega)$ by using empirical models. The symmetric $\chi''(\omega)$ can be conveniently represented by the Cole-Cole expression:[6,7].

$$\chi(\omega) = \chi'(\omega) + i\chi''(\omega) = \frac{x_0}{1+i\omega\tau_\epsilon} \quad \text{(S2)}$$

where $\chi_0$=NV$^2$M$^2$/K$_B$T is the static susceptibility of the sample comprising N monodisperse particles of volume V with a saturation magnetization M. The single relaxation time indicates the monodisperse particle. The AC susceptibility curve of FePt @IONP exhibits a symmetric

Debye peak, shown in **Figure S8**, indicating a suspension of monodisperse nanoparticles. The fitted relaxation time is $\tau_e = 1.3\times10^{-5}$ sec. On the other hand, the AC susceptibility of IONP exhibits a structure with features fitted by two relaxation times ( $\tau_{e1}=2\times10^{-5}$ sec. and $\tau_{e2}=1.8\times10^{-4}$ sec.).

According to ref. [8], the effective relaxation time of $\sim10^{-5}$ sec corresponds to the particle size in the range of 15 to 20 nm. The larger particle or cluster size leads to the longer relaxation time. Our TEM images shown in Figure 2 of manuscript reveal that both of IONPS and FePt@IONPs have the particle sizes in this range and no obvious difference of size distribution for those two samples. Therefore, the longer relaxation time of IONPs ( $\tau_{e2}=1.8\times10^{-4}$ sec) may suggest that a strong dipole interaction exists among IONPs, leading to lager magnetic clusters.

S 9: Micromagnetic simulations of the domain structure of (a) IONP and (b) FePt@IONP nanocube system

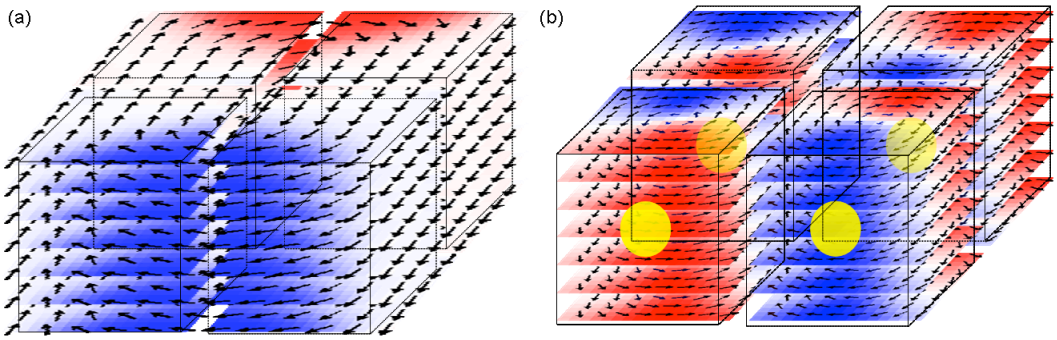


**Figure S9**. The OOMMF simulation for three-dimensional visualization of the magnetic moment within an assembly of four nanocubes. (a) Four $Fe_3O_4$ nanocubes form a flux closure state among nanocubes and (b) FePt@IONPs show that the presence of the core stabilizes the vortices in each cube.

The lateral sizes of the NPs were extracted from TEM images (the size of cubic IONPs is16.1nm; cubic FePt@$Fe_3O_4$ is 14.7nm with FePt core of 4nm). We use the micromagnetic OOMMF code to set the 3D magnetic configuration of the sample. The bulk saturation magnetization Ms ($Fe_3O_4$:$4.71\times10^5$ A/m, FePt: $1.14\times10^6$ A/m), exchange constant ($Fe_3O_4$:$0.3\times10^{-12}$ J/m), cubic anisotropy constant ($Fe_3O_4$:$0.1\times10^5$ J/m$^3$) and uniaxial anisotropy (FePt:$7\times10^6$ J/m$^3$) were used for simulation parameters. The damping parameter of $\alpha$= 0.5 was used to reach the equilibrium remanent state rapidly. The direction of the magnetic induction is indicated by black arrows. The OOMMF simulations for the remanent state reveal that the domain structure of core-shell FePt@IONP nanocubes exhibits a vortex state in each nanoparticle, analogously to the observed electron holography fringe patterns [9,10,11]. The induction state of IONPs shows strong interaction between adjacent nanocubes.

S 10: Shape evolution of magnetic nanoparticle assembly with or without a DC magnetic field

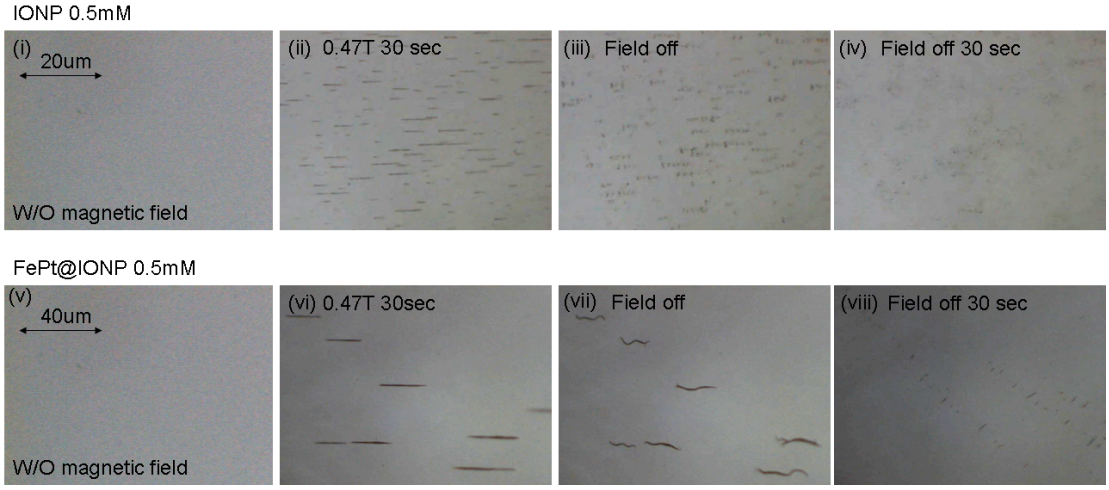


**Figure S10**. Shape evolution of magnetic nanoparticle assembly with or without DC magnetic field of 0.47 T by using optical microscopy.

Under the application of DC magnetic field, the magnetic particles can be assembled into different configurations [12, 13, 14, 15]. In our case, we set the DC magnetic field equal to 0.47 T. For IONPs: (i) well-dispersed nanoparticles without magnetic field; (ii) when the magnetic field of 0.47T was applied for 30 seconds, the chain clusters are formed and aligned along the magnetic field direction; (iii) when the magnetic field was turned off, the chain disappeared and a few clusters appeared in the aligned directions; (iv) at 30 seconds after turning off the magnetic field, the IONPs are re-dispersed. If water is slightly disturbed, IONPs can be well-dispersed in the solution, as shown in (i).

For FePt@IONPs: (v) the well-dispersed nanoparticles without magnetic field; (vi) when the magnetic field of 0.47T was applied for 30 seconds, the chain clusters are formed and aligned in the same direction as the field; (vii) when the magnetic field was turned off, the chain was still present but with distorted shapes; (viii) at 30 seconds after turning off the magnetic field, short-range chains remained. If water is slightly disturbed, FePt@IONPs can be well-dispersed in the solution, as in (v).

S 11: The AC susceptibility spectra for IONPs and FePt@IONPs in solution with or without a magnetic field

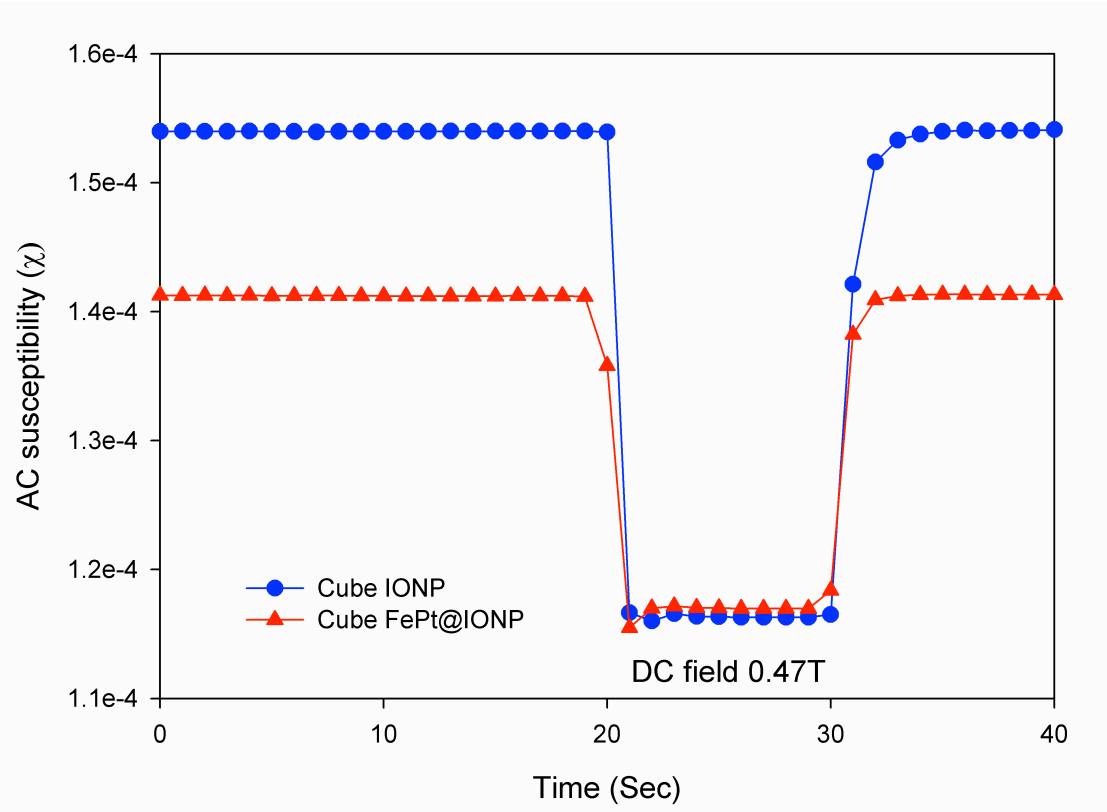


**Figure S11**. AC susceptibility spectra at 25 KHz of cube IONPs and FePt@IONPs with and without the DC magnetic field of 0.47T. The concentration of the sample is 0.1mg/ml. Here, the DC field is turned on and off at the 20$^{th}$ and 30$^{th}$ sec, respectively. With the applied filed, the nanoparticles aggregated, leading to reduced susceptibility. The reversible spectra indicate that both IONPs and FePt@IONPs can be re-dispersed after removing the DC field.

When the DC field is applied, the AC susceptibility of IONPs and FePt@IONPs in solution is reduced, as shown in **Figure S11**. When the field is removed, in both cases the AC susceptibility is raised to their original values. AC susceptibility can be reduced due to the formation of magnetic clusters [16]. When DC magnetic field was applied, aggregation of nanoparticles may occur, leading to a significant reduction in AC susceptibility. After removal of the DC field, the raised AC susceptibility indicates that the nanoparticles are well dispersed in the solution again.

S 12: Monte Carlo simulation of proton dephasing signal for continuous and discontinuous chains in large structures

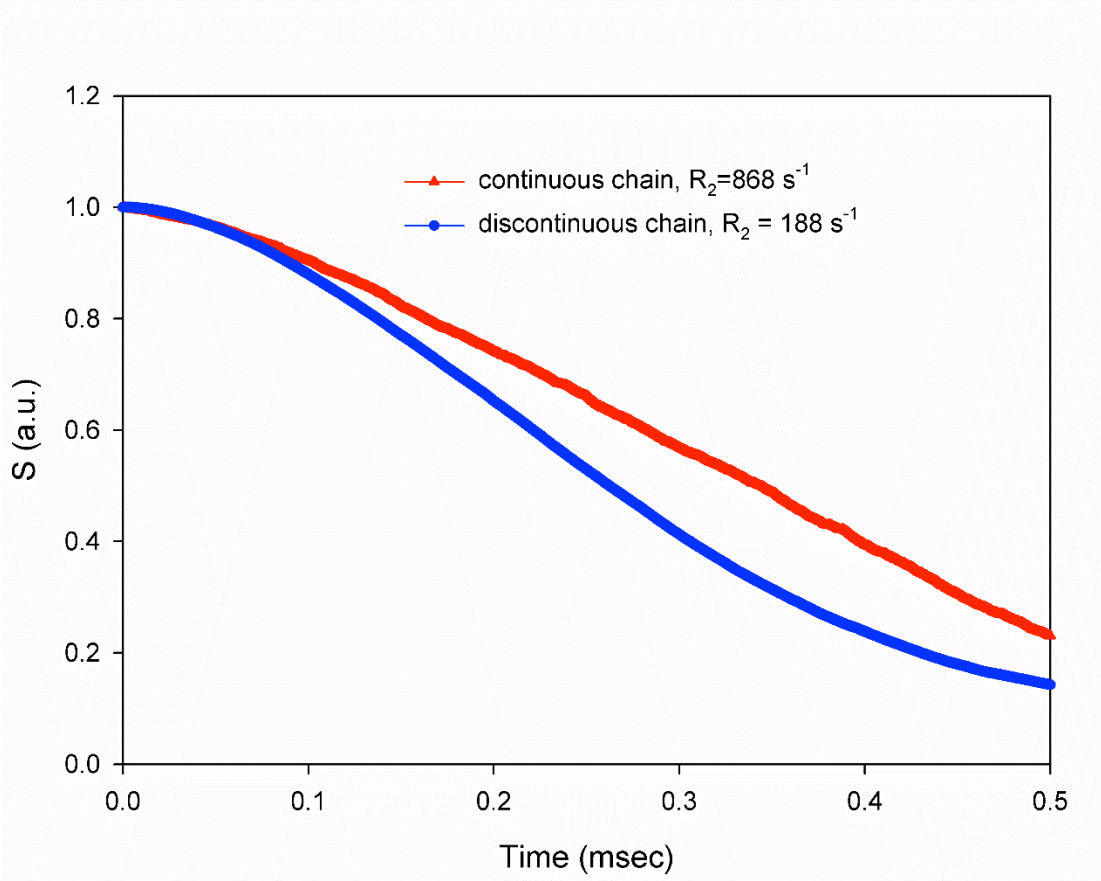


**Figure S12**. Proton dephasing signal S for two systems: continuous chains (blue curve) and discontinuous chains (red curve). The proton dephasing signal for large structures of continuous chain of 3636 magnetic nanoparticles (6x1x606 particle in xyz direction) and discontinuous chains of 101 magnetic clusters with each composed of 36 magnetic nanoparticles.

We consider a number of protons (Np) moving in a system with cubic Ns ($Fe_3O_4$ or FePt@$Fe_3O_4$). The dephasing of the proton moment S(t) is given by[17, 18]:

$$S(t+\Delta t) = \frac{1}{N_p}\sum_{i=1}^{N_p} cos(\varphi_i(t) + \Delta\varphi_i) \quad \text{(S3)}$$

$\varphi_i(t)$ is the angle with respect to the $z$ direction.

$$\Delta\varphi_i = \gamma B(r)\Delta t \quad \text{(S4)}$$

$\gamma$ is the gyromagnetic ratio of hydrogen ($2.67\times10^8$ rad/sT). When calculating the net magnetic

field B due to the presence of nearby nanoparticles, only particles within distance of the proton are considered. The net magnetic field B can be expressed as:

$$B(r) = \frac{\mu_0 M}{3}\left(\frac{a}{r}\right)^3(3\cos^2(\theta) - 1)) \quad \text{(S5)}$$

where $\mu_0$ is the permeability of free space ($4\pi\times10^{-7}$ H/m), *M* is the magnetization of the particle*r* is the distance from the particle center, θ is the angle with respect to the *z* direction and *a* is the size of the cubic nanoparticles. When the echo spacing is small, S(t) can be expressed by

$$S(t) = M \cdot exp\left(\frac{-t}{T_2}\right) \quad \text{(S6)}$$

where *t* is the overall time from the excitation to a particular echo we are measuring. S(t) has an exponential decay form with time.

Because of computational time, the simulation results shown in Figure 5 were done for small structures with a limited number of nanoparticles (total ~1500 nanoparticels). Our results illustrate the importance of the local configuration not just the global packing fraction. The relaxation rate depends also on the number of particle per cluster, on the local cluster density and the spacing between clusters. We performed also simulation for larger structures to ensure magnetic nanoparticle configuration more similar to experimental samples. The results are shown in **Figure S12**.

The configuration is set for the discontinuous and continuous chain structure, with each structure containing 3636 particles (total ~ 363600 nanoparticles). Due to large structures, the calculations are limited to a packing density of 0.001. From the curve fitting in the equation S6, the $R_2$ ($R_2=1/T_2$) of continuous chain is 868 $s^{-1}$, higher than discontinuous chain (188 $s^{-1}$) in the same packing density (Figure S12). Qualitatively the behavior is the same as for small clusters, in terms that the continuous chain has a larger $R_2$ than the discontinuous chain. Quantitatively, the values are smaller in comparison with the small structure system for

packing density of 0.001 (Figure 5). To compare the simulation results with the experimental data shown in Fig 1a, we extrapolate the $R_2$ value to 2mM Fe concentration (corresponding to packing density of 0.001) with the same linear relationship, the estimated $R_2$ values are 727 $s^{-1}$, 260 $s^{-1}$ for FePt@IONPs continuous chains and IONPs discontinuous chains. On the other hand, the simulated values for the small structure are 1231$s^{-1}$ and 415$s^{-1}$, respectively. For larger structures, the simulation results are closer to the real case.

S 13: Particle size enhanced relaxivity for FePt@IONPs

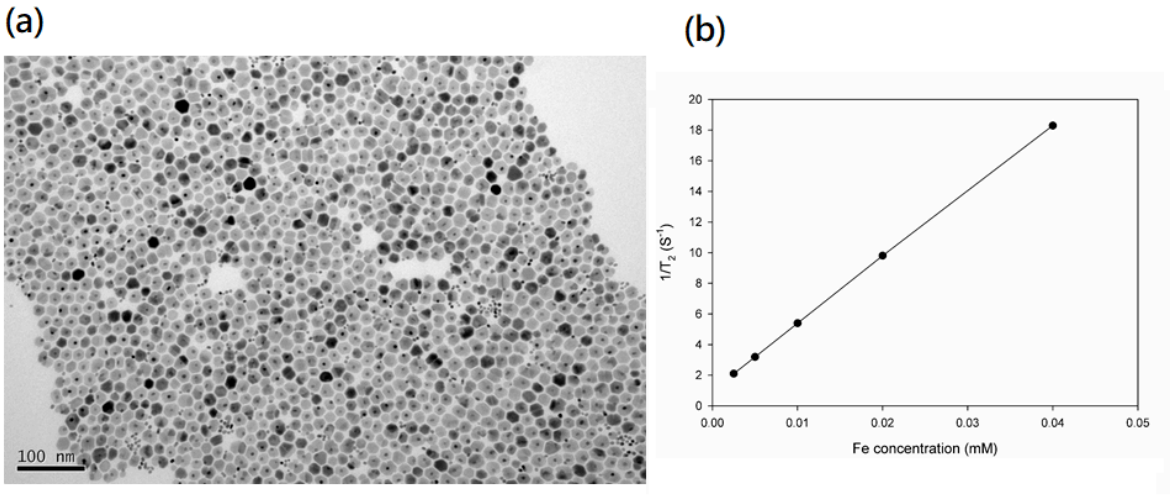


Figure S13. (a) TEM image of FePT@IONP and (b) relaxivity measurement with $1/T_2$ vs. Fe concentration.

By tuning the temperature of synthesis process, we can change the core-shell particle size. With increased size (17.8 nm) of superparamagnetic core-shell structure, we can further improve the relaxivity to 411.3 $mM^{-1}s^{-1}$, as shown in Figure S13. Although when the size is increased, the uniformity of NP becomes more difficult to control, our approach can still reach even higher $r_2$ by further optimization.

Supplementary Movie captions

**Movie S1**: The optical microscope movie was captured by charge-coupled device (CCD) cameras. Under the in-plane DC magnetic field of 0.47T, FePt@IONPs are aligned in the same direction as the DC field. The DC magnetic field is always applied during 5 seconds. The applied orthogonal AC pulse field (0.5 mT at 20 MHz) does not disturb the continuous chains of FePt@IONPs.

**Movie S2**: IONPs is aligned by the DC magnetic field of 0.47T. The applied orthogonal AC pulse field (0.5 mT at 20 MHz) disturbs the IONPs chains at regular intervals. The IONPs become discontinuous chains when AC pulse field is applied.

References

[1] J. P. Fortin, C. Wilhelm, J. Servais, C. Ménager, J. C. Bacri, F. Gazeau, *J. Am. Chem. Soc.* **2007**, 129, 2628.

[2] M. Suto, Y. Hirota, H. Mamiya, A. Fujita, R. Kasuya, K. Tohji, B. Jeyadevan, *J. Magn. Magn. Mater.* **2009**, 321, 1493.

[3] S. Dutz, R. Hergt, *Int. J. of Hyperthermia* **2013**, 29, 790.

[4] J. H. Lee, J.T. Jang, J. S. Choi, S. H. Moon, S. H. Noh, J. W. Kim, J. G. Kim, I. S. Kim, K. I. Park, J. W. Cheon, *Nat. Nanotechnol.* **2011**, 6. 418.

[5] B. G. Veronica, S. P. Regino, J. T. F. María, *J. Mater. Chem.* **2012**, 22, 2992.

[6] P.C. Fannin, B. K. P. Scaife, S. W. Charles, *J. Mag. Mag. Mat.* **1988**, 72, 95.

[7] K. S. Cole, R. H.Cole, *J. Chem. Phys.* **1941**, 9, 341.

[8] V. Singh, V. Banerjee, M. Sharma, *J. Phys. D: Appl. Phys.* **2009**, 42, 245006

[9] J. M. THOMAS, E. T. SIMPSON, T. KASAMA, R. E. DUNIN-BORKOWSKI, *Acc. Chem. Res.* **2008**, 41, 665.

[10] E. Snoeck, C. Gatel, L. M. Lacroix, T. Blon, S. Lachaize, J. Carrey, and M. Respaud, B. Chaudret, *Nano Lett.* **2008**, 8, 4293.

[11] L. M. Lacroix, S. Lachaize, F. Hue, C. Gatel, T. Blon, R. P. Tan, J. Carrey, B. Warot-Fonrose, B. Chaudret, *Nano Lett*. **2012**, 12, 3245.

[12] G. Singh, H. Chan, T. Udayabhaskararao, E. Gelman, D. Peddis, A. Baskin, G. Leitus, P. Král, R. Klajn, *Farad. Discuss.* **2015**, 181, 403.

[13] S. A. Corr, S. J. Byrne, R. Tekoriute, C. J. Meledandri, D. F. Brougham, M. Lynch, C. Kerskens, L. O'Dwyer, Y. K. Gun'ko, *J. Am. Chem. Soc.* **2008**, 130, 4214.

[14] S. Singamaneni, V. N. Bliznyuk, C. Binek, E. Y. Tsymbal, *J. Mater. Chem.* **2011**, 21, 16819.

[15] H. Jaganathan, D. L. Hugar, A. Ivanisevic, *ACS Appl. Mater. Interfaces* **2011**, 3, 1282.

[16] C.Y. Hong, C.C. Wu, Y.C. Chiu, S.Y. Yang, H. E. Horng, H. C. Yang, *Appl. Phys. Lett.* **2006**, 88, 212512.

[17] H. W. de Haan, *Magn. Reson. Med.* **2011**, 66, 1748.

[18] R. A. Brooks, F. Moiny, P. Gillis, *Magn. Reson. Med.* **2001**, 45, 1014.